Applied Energy 401 (2025) 126754

Contents lists available at ScienceDirect

Applied Energy

journal homepage: www.elsevier.com/locate/apenergy

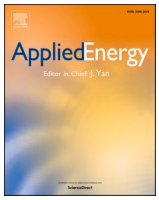

Experimental demonstration of in-situ cracked premixed swirl NH_3-air flames

B. Aravind *, Sivachidambaram Sadasivam, Jordan Davies, Syed Mashruk, Agustin Valera-Medina

College of Physical Sciences and Engineering, Cardiff University, Wales CF24 3AA. UK

HIGHLIGHTS

- A novel multi-pass heat exchanger cracker was developed for in-situ cracking.
- In-house electroplated mesh matched commercial catalyst performance-cost-effective.
- Detailed catalysts characterization and emission-flame topology analysis conducted.
- The concept supports 'X-to-Power' applications, advancing the NH_3-H_2 agenda.

ARTICLE INFO

Keywords:
Clean energy
Global emission
Hydrogen
Ammonia
X-to-power
Cracking efficiency
Heat exchanger

ABSTRACT

This study investigates the in-situ thermo-catalytic cracking of ammonia (NH_3) and the combustion characteristics of the resulting cracked flame. A swirl-stabilized burner equipped with a novel multi-pass heat exchanger and a catalytic tube was employed to analyse NH_3 cracking and combustion. Five catalysts were evaluated, including three developed in-house-ruthenium (Ru) and cobalt (Co) electroplated on stainless steel wire mesh, and Ru nanoparticles loaded onto sodium zeolite along with two commercially available alumina-based Ni and Ru pellets. The performance of thermal cracking is then compared to thermo-catalytic cracking. The cracking efficiency decreased inversely with NH_3 flow rate, from 70 % to 17 % at 773-813 K and 100 % to 60 % at 893–932 K, with Ru-based catalysts outperforming thermal cracking by 20 % at 35 SLPM of NH_3. At 773–813 K, both electroplated Ru and Ru—Co stainless steel mesh configurations performed similarly, indicating that catalyst contact time can be further optimised. The stability and emissions of the cracked flames were assessed at air flow rates of 100–200 SLPM. The cracking efficiencies of 54–58 %, 61–62 %, and 58–65 % were observed at 798–825 K, 836–857 K, and 878–901 K for cracker flow rates of 15, 20, and 25 SLPM respectively. Emissions analysis revealed increasing N_2O levels with higher air flow and NO peaks at an equivalence ratio between 0.74 and 0.83. Flame instabilities under lean conditions led to NH_3 slip. These findings highlight the need for catalyst optimisation to enhance NH_3 cracking efficiency, improve flame stability, and reduce emissions, advancing sustainable combustion technologies.

1. Introduction

The global initiative to transition from fossil fuels to carbon-free or low-carbon alternatives has garnered significant attention from researchers, alongside the advancements made in combustion technologies [1,2]. Ammonia (NH_3) is recognised for its potential as a clean energy source due to its characteristics as a carbon-free fuel and an effective hydrogen (H_2) carrier [3,4]. The recent techno-economic analysis of NH_3 highlights its potential as a viable fuel for the power generation and transportation sectors, citing reduced transportation and storage costs, a well-established infrastructure, and enhanced safety measures [5–8]. Nonetheless, employing NH_3 presents certain challenges, including its slow combustion rate, high autoignition temperature, and the potential for NO_x emissions under conventional operating conditions [9,10]. To address these challenges, various combustion enhancement techniques such as cofiring with highly reactive fuels

* Corresponding author.
E-mail address: balakrishnana4@cardiff.ac.uk (B. Aravind).

https://doi.org/10.1016/j.apenergy.2025.126754
Received 12 February 2025; Received in revised form 30 July 2025; Accepted 11 September 2025
Available online 20 September 2025

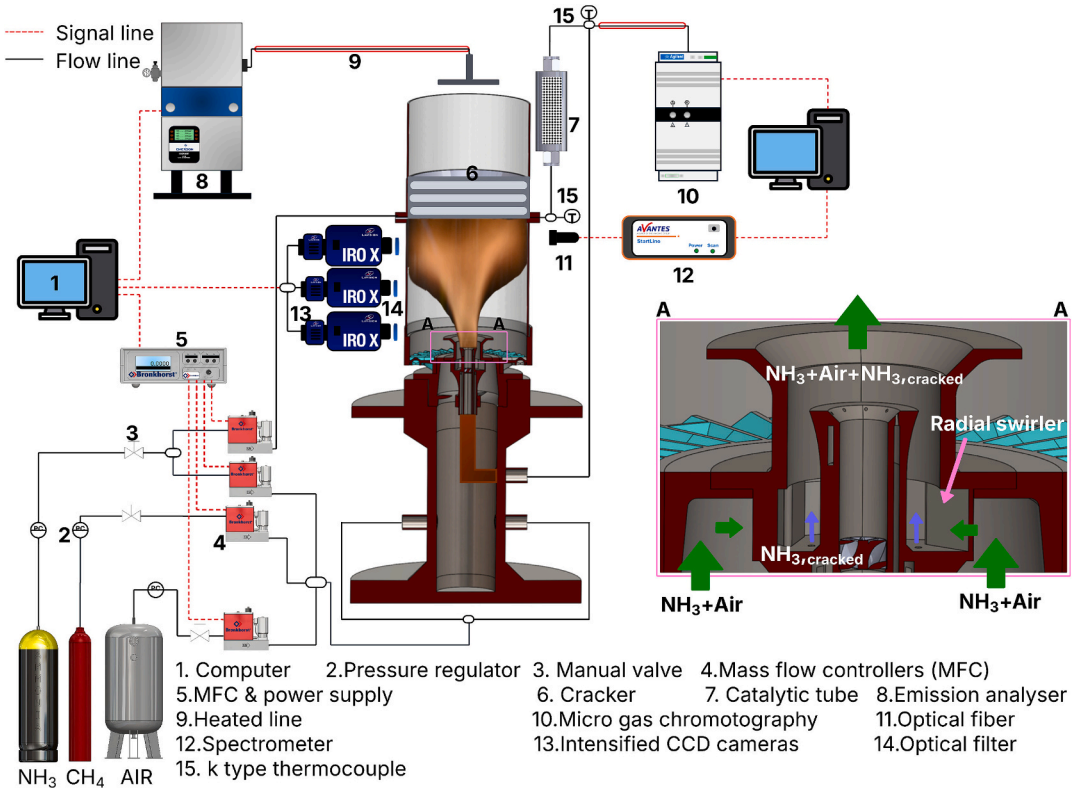

Fig. 1. Schematic of the experimental setup.

[11,12], staged combustion [13,14], pre-cracking [15], stratification [16], plasma assisted combustion [17] are generally employed. Among them, cofiring NH_3 with methane [18,19] and H_2 [20] are widely adopted strategy as it requires minimal modification to the combustion chamber. The idea of on-site NH_3 cracking is attractive as it removes the necessity for transporting and storing H_2 [21,22]. Compared to co-firing H_2, directly utilizing partially cracked NH_3 eliminates the need to separate H_2 from the resulting H_2-nitrogen mixture. This separation process is both economically inefficient and technically challenging due to the similar molecular sizes and quadrupole moments of H_2 and N_2, as well as the relatively low Knudsen selectivity between the two gases [23]. However, a major drawback of this approach is the potential increase in NO_x emissions as compared to other strategies. Nevertheless, this issue can be effectively mitigated through de-NOx after-treatment methods. Additionally, Davies et al. [24] recently demonstrated that a 20 % cracked NH_3 blend significantly reduced NO, NO_2, and N_2O emissions at the expense of NH_3 under rich conditions as compared to the more commonly studied 70/30 (vol%) NH_3-H_2 blend. Although numerous studies [24–26] have examined simulated NH_3/H_2 and $NH_3/H_2/N_2$ mixtures, there has been a lack of thorough investigation into the practical implementation of in-situ NH_3 cracking within mGT applications.

Nickel (Ni), Cobalt (Co), Iron (Fe), and Ruthenium (Ru) based catalysts have been commonly studied for NH_3 cracking, with Ru-based catalysts showing promising H_2 conversion rates [27]. A Ni_5Co_5/SiO_2 catalyst, with a Ni/Co molar ratio of 5:5, demonstrated an impressive NH_3 conversion rate of 76.8 % at 550 °C with a gas volumetric flow rate of 30,000 mL/h. Notably, even when the reaction temperature was increased to 650 °C, satisfactory conversion rates were still achieved [28]. The performance of ruthenium-based catalysts has been enhanced through the incorporation of secondary metals and the use of diverse supports. Fe-supported Ru cluster catalysts on porous and graphitic carbon demonstrated an impressive 97.5 % conversion of NH_3 [29]. The results demonstrated that the Ru/Fe catalyst is exceptionally efficient in generating carbon-free H_2 from NH_3. The literature suggests several avenues for future research, particularly focusing on the creation of cost-effective, high-efficiency catalysts and advancements in reactor design [30]. Edison et al. [31] successfully loaded ruthenium nanoparticles onto stainless steel mesh using deep eutectic solvents for the H_2 evolution reaction. Previous research has looked into the methods for applying catalytic converter coatings to stainless steel wire mesh for use in industrial applications [32]. Zeolite, a naturally occurring aluminosilicate mineral, was also studied as support for Ru catalysts used in H_2 production [33,34]. The current study compares the H_2 conversion percentages of Ru and Ru/Co electroplated stainless steel wire mesh, as well as Ru nanoparticles supported by zeolite, to commercially available alumina-supported Ni and Ru catalysts.

To date, existing literature has predominantly focused on the combustion characteristics of simulated cracked NH_3 flames. However, there remains a notable absence of studies on combustion characteristics of real cracked NH_3 flame, which holds greater practical relevance of the present study. This study aims to bridge this gap between simulated and real cracked NH_3 flames, thereby providing essential data for advancing the practical deployment of NH_3 as a combustion fuel.

In this study, a novel multi-pass heat exchanger cracker was developed for in-situ thermo-catalytic cracking. A detailed material characterization of the catalysts and an in-depth emission and flame topological analysis of the in-situ cracked flames are envisaged for a wide range of operating conditions. The novelty of our study is highlighted as follows (1) The first study to demonstrate an in-situ cracked NH_3 flame with exhaust gas recovery in a gas turbine model combustor. (2) The development of an inexpensive, in-house Ru-based catalyst with high cracking efficiency outperforming the similar commercially available catalysts. (3) The first comprehensive analysis of the combustion characteristics of real cracked NH_3 flames, serving as a pivotal reference for future simulated studies. Furthermore, this concept can be used for "X-to-Power" applications, supporting the NH_3-H_2 agenda.

2. Experimental details

2.1. Experimental setup

The experiments were carried out using a novel generic swirl burner from Cardiff University's Centre for Excellence in Ammonia Technologies (CEAT) [35]. Fig. 1 shows a schematic of the experimental setup. High-precision Bronkhorst mass flow controllers were used to control NH_3, CH_4, and air flows, achieving an accuracy of ±0.5 % within 15–95 % of the full scale. The NH_3-CH_4-air mixture was fed into the plenum through two inlets, depending on the operating conditions. The mixture is then circulated through the annular gap between the burner nozzle (d = 31.5 mm) and bluff body (d = 22.5 mm) using a radial swirler with a swirl number of 1.45. For more information on the burner's dimensions, see Sato et al. [12].

A novel multi-pass heat exchanger cracker was installed longitudinally to the burner, 150 mm from the burner rim, to capture heat from the hot combustion exhaust. The cracker unit comprises of two coaxial ring structures, each designed to facilitate few sequential passes of the NH_3 flow to extract maximum heat from the exhaust gas. The preheated or partially cracked NH_3 is then directed into the catalytic tube, which contains various catalysts. The cracker's dimensional details are not disclosed due to intellectual property concerns and therefore the heat transfer analysis. The flame confinement system has a diameter of 160 mm and a total length of 300 mm, including the quartz tubes (GE214, transmissivity of 85 % at UV range) on each axial side of the cracker.

A portion of the cracked NH_3 is drawn out by an analytical diaphragm pump (MP26/JH1 M&C) and sent to an Agilent 990 microGC to measure $NH_3/H_2/N_2$ from the cracking process in real time. The remainder is fed to the combustion chamber via axial holes in the swirler unit (shown in the inset of Fig. 1). A K-type thermocouple is used to measure the temperature just before the catalytic tube. A bespoke Emerson CT5100 quantum cascade laser gas analyser was used to measure exhaust emissions such as NO, N_2O, NO_2, NH_3, O_2, and H_2O at 1 Hz with ±1 % repeatability and 0.999 linearity. To prevent NH_3 condensation and ensure accurate sampling, a heated line from Winkler was maintained at 463 K throughout the measurement process. To ensure consistent and reliable emission analysis, especially NO_2 measurements, a cross-shaped probe with equidistant holes for homogeneous sample collection was placed 25 mm above the quartz exit to prevent interaction between the surrounding air and the exhaust gas. Therefore, the current NO_2 measurements reflect only the NO_2 present in the exhaust gas itself [36]. Measured oxygen was negligible at stoichiometric conditions, demonstrating that no outside air was entrained into the sampling probe. All measuring equipment was calibrated and verified for accuracy before every experimental campaign began. Each experimental case was repeated at least three times to ensure the repeatability of the results. The error bars are plotted based on the standard deviation similar to our previous studies [11,24]. The emission and temperature measurements were recorded only after steady-state conditions were reached. The emissions data were collected for 120 s at a frequency of 1 Hz then time-averaged and normalised to a 15 % oxygen (dry) condition, while temperature data were collected for 10 min at the same frequency for calculation of mean and standard deviation.

The flame chemiluminescence images were captured using three LaVision CCD cameras simultaneously at a frequency of 10 Hz. The OH* ($A^2\Sigma^+$–$X^2\Pi$ system), NH* ($A^3\Pi$–$X^3\Sigma$ − system) and NH_2* (single peak of the NH_2 α band) [37] is collected using 309 nm bandpass filter (±10 nm FWHM), 336 nm band pass filter (±10 nm FWHM), and 630 nm (±10 nm) bandpass filters, which are mounted to the cameras. For each test point, 200 frames were captured with LaVision Davis v10, time-averaged, background-corrected, and deconvolved using the Abel transformation in MATLAB [38]. Furthermore, the chemiluminescence spectrum of the flame at 25 mm above the burner's exit and 100 mm from its central axis was recorded using a flexible AvaSpec-ULS spectrometer.

Table 1
Catalysts used in the current study.

Name of the Catalyst	Type	Chemical composition	Amount used/ Configuration in the catalytic tube
Ni pellets	Commercially obtained from Heraeus.	10 % Ni/Al_2O_3.	100 g of material.
Ru-pellets	Commercially obtained from Heraeus.	10 % Ru/Al_2O_3	100 g of material.
Ru-mesh	Prepared for current study.	Thin coated Ru on a stainless-steel wire mesh (The coating contains 20 % Ru; semi-quantitative)	200 meshes (The mass percentage of Ru is negligible as coated as thin oxides).
Ru-Co-mesh	Prepared for current study.	Thin coated on the wire mesh (the coating contains 4.6 % Co and 4 % Ru; semi-quantitative)	200 meshes (The mass percentage of Ru and Co is negligible as coated as thin oxides).
Ru-Zeolite	Prepared for the current study.	Na-zeolite, Na- ion exchanged by Ru, and 10 % Ru mass basis.	5 g of material.

This study covered two different types of experiments. The first experiment compared the performance of various catalysts at varying cracker temperatures. Initially, a 5 kW CH_4-air flame was ignited. To achieve the desired testing temperature at the cracker outlet for different NH_3 flow rates (V_{NH3},crack), a blend of CH_4-NH_3 (main NH_3) and air were supplied. Cracked NH_3 was fed back into the burner. In the second experiment, the combustion performance of the in-situ cracked flame was investigated at different air flow rates and thermal powers. To initiate NH_3 cracking, a CH_4-air flame was first established to achieve the cracker outlet temperature of at least 700 K. The CH_4 flow rate was gradually reduced to zero, and NH_3 was added alongside the cracked NH_3 flow resulting in a stable partially cracked NH_3 flame.

2.2. Preparation of catalysts

Three types of Ru-based catalysts were prepared; (1) Ruthenium coated stainless steel (Ru-mesh), (2) Ruthenium-Cobalt coated stainless steel mesh (Ru-Co-mesh) and (3) Zeolite supported ruthenium (Ru-zeolite). The Ru-mesh and Ru-Co-mesh were prepared by electroplating stainless-steel wire meshes with each having a 0.25 mm opening, 0.16 mm wire diameter, and 25.4 mm mesh diameter, with each mesh weighing approximately 0.27 g. A total of 200 coated wire mesh pieces were arranged within a cylindrical catalytic tube, which had an outer diameter of 28.1 mm, an inner diameter of 25.4 mm, and a length of 200 mm (see Fig. 1. No.7: Catalytic tube).

A y-sodium (Na)-zeolite (ID: CBV100) characterised by a SiO_2/Al_2O_3 molar ratio of 5.1, a surface area of 900 m^2/g, and a Na mass percentage of 10 % was utilised in the preparation of the Ru-zeolite catalyst. The Ru-zeolite was prepared by the ion-exchange method by replacing the Na from Zeolite by Ru ions. Five grams of Ru-zeolite were utilised within the catalytic tube, with the powder evenly distributed at one gram per wire filter across five filters arranged at 40 mm intervals (refer to Fig. 1. No.7: Catalytic tube).

The surface morphology and semi-quantitative elemental analysis of Ru-Co-mesh and Ru-Co-mesh samples were performed using a Zeiss Sigma HD Field Emission Gun Analytical Scanning Electron Microscope (ASEM) and Oxford Instruments energy dispersive X-ray spectrometers (EDS), and the findings are detailed in results and discussion section. The zeolite and Ru-zeolite samples were characterized using a JEOL JEM-2100 scanning transmission electron microscope to verify the presence of ruthenium on the zeolite structure. PerkinElmer infrared

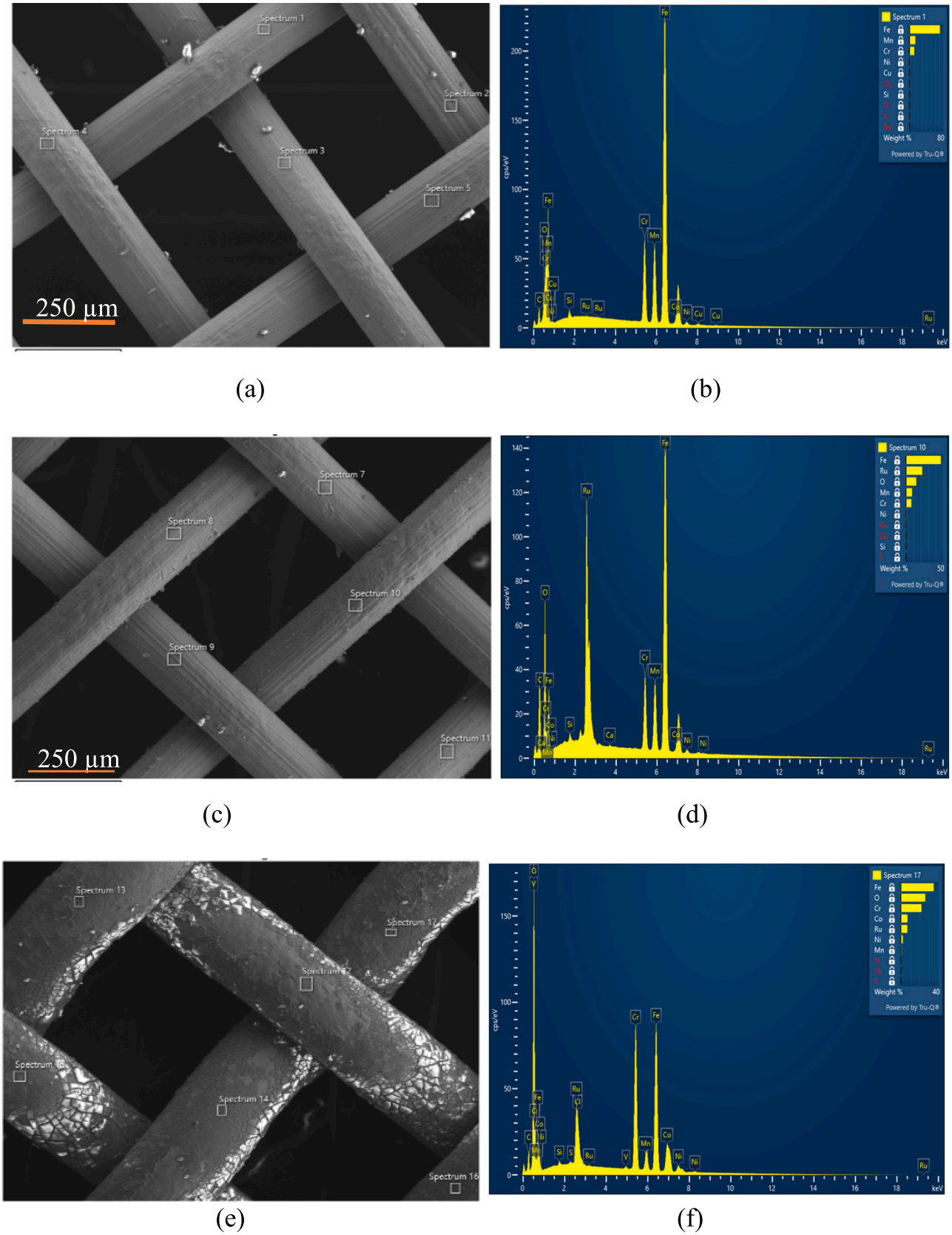

Fig. 2. SEM and EDS spectrum showing stainless steel mesh (a & b), uniform distribution of Ru on the Ru-mesh (c &d), and Ru-Co-mesh (e &f).

Table 2
Semi-quantitative chemical composition analysis of the stainless-steel mesh, Ru-mesh and Ru-Co-mesh.

Element/ mass %	O	Si	S	Cr	Mn	Fe	Co	Ni	Cu	Ru
SS Wire mesh	0.76	0.52	0.02	11.29	13.86	71.04	0.59	1.19	0.73	0.01
Ru-mesh	11.03	0.28	0.03	8.22	8.73	50.12	0.40	0.82	0.43	19.95
Ru-Co-mesh	15.51	0.29	0.08	20.77	1.22	48.66	4.64	4.60	0.20	4.03
Ru-mesh (exposed to NH_3)	5.06	0.36	0.1	12.75	10.83	50.08	–	2.21	0.11	15

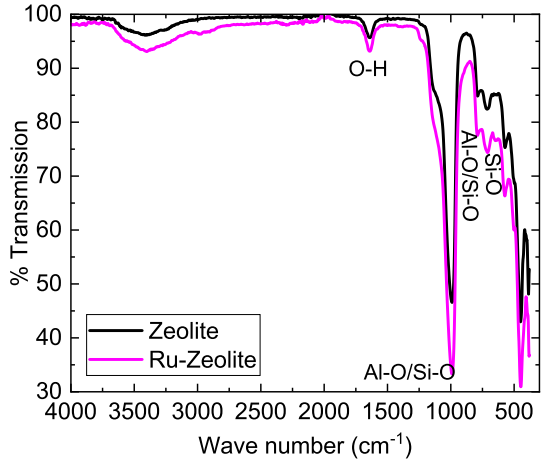

Fig. 3. FTIR images of zeolite and Ru-zeolite show no structural change.

absorption spectroscopy was used to verify the Ru-zeolite and y-sodium zeolite structure integrity before and after loading of the Ru ions.

The aforementioned catalysts' NH_3 cracking efficiency was analysed comparatively against commercially available alumina-supported nickel (Heraeus 10 % Ni/Al_2O_3, 100 g), and ruthenium pellets (Heraeus 1.35 % Ru/Al_2O_3, 100 g). Table 1 presents the catalysts utilised in the investigation along with their respective characteristics.

3. Results and discussion

3.1. Performance of the cracker system

3.1.1. Morphology and semi-quantitative analysis of the Ru-mesh, Ru-Co-mesh, and Ru-zeolite

Fig. 2 illustrates an example of surface morphology, along with the energy dispersion spectrum (EDS) of the Ru-mesh. The chemical composition of the stainless-steel mesh, Ru-mesh, and Ru-Co-mesh is presented in Table 2. The SEM and EDS image presented in Fig. 2 illustrates a uniform distribution of Ru across the surface of the stainless-steel mesh, with an elemental mass percentage of 20 % as detailed in Fig. 2 and Table 2. The measurement of the surface coating and the few nanometer depths of the stainless-steel wire should not be utilised to ascertain the elemental composition of the entire wire mesh. It is essential to take into account the interference from the Fe wire and the variations in surface coating thickness. The co-deposition of Co—Ru resulted in a diminished mass percentage of 4 % as indicated in Table 2. The analysis of morphology and EDS reveals a non-uniform distribution of Co and Ru on the wire surface. Variations in electrochemical reactions, electrolyte behaviour, and current density can lead to non-uniformities in electroplating processes. The mass of the wire mesh exhibited minimal variation during the coating process in comparison to its state prior to treatment. For example, the weight of 38 wire meshes were about 10.4 g both prior to and following the coating process. The SEM-EDS analysis and mass balance indicated that Ru and Co were present as thinly coated layers, with the overall mass being considerably

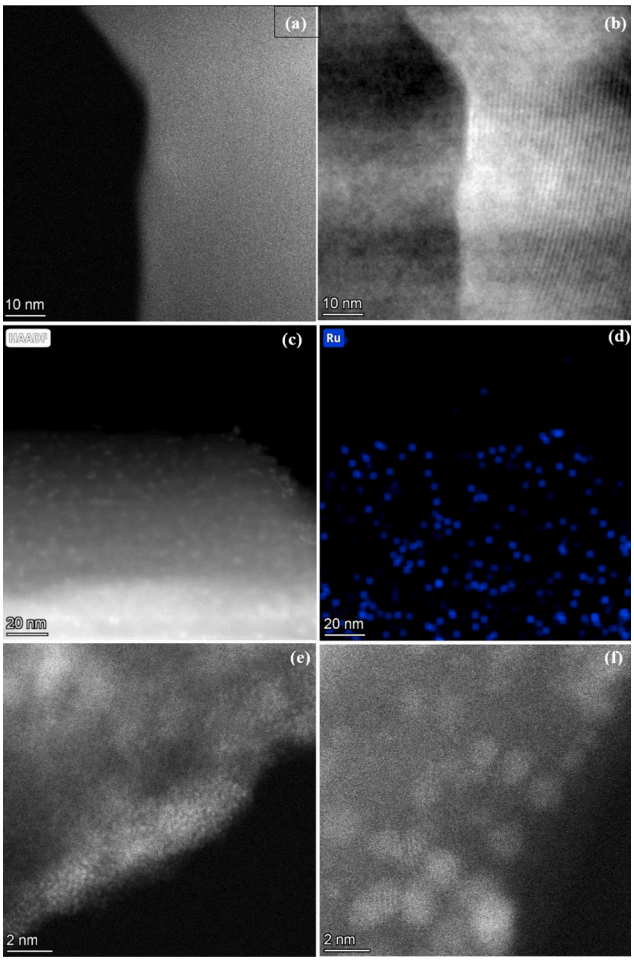

Fig. 4. HAADF image (a) and iDPC image (b) showing atomic lattice of zeolite support. HAADF image (c) and corresponding EDX map (d) showing location of Ru signal on zeolite support. Image (e) and (f) show Ru atoms aggregated near edge of support. (Insert: approximately 1–2 nm size Ru particles).

less than that observed in commercial catalysts. As noted earlier, each of the alumina-based catalysts comprised 10 grammes of Ni and Ru. Interestingly, the integrity of the metal mesh and Ru coating remained intact throughout the entire experimental campaign. However, elemental analysis revealed a slight reduction in surface Ru content, with approximately 15 % present on the surface compared to 20 % in unexposed samples. This discrepancy may be attributed to the removal of a portion of the surface coating due to high-velocity impacts or variations occurring during the electroplating process itself. Given that this represents a qualitative assessment, the Ru-mesh is regarded as reusable.

The FTIR spectrum of zeolite and Ru-Zu showed that the zeolite structure was intact despite the ion exchange reaction (Fig. 3). This has been confirmed by the TEM analysis, whilst atomic lattices were visible in pure zeolite, however expected zeolite channels were not visible

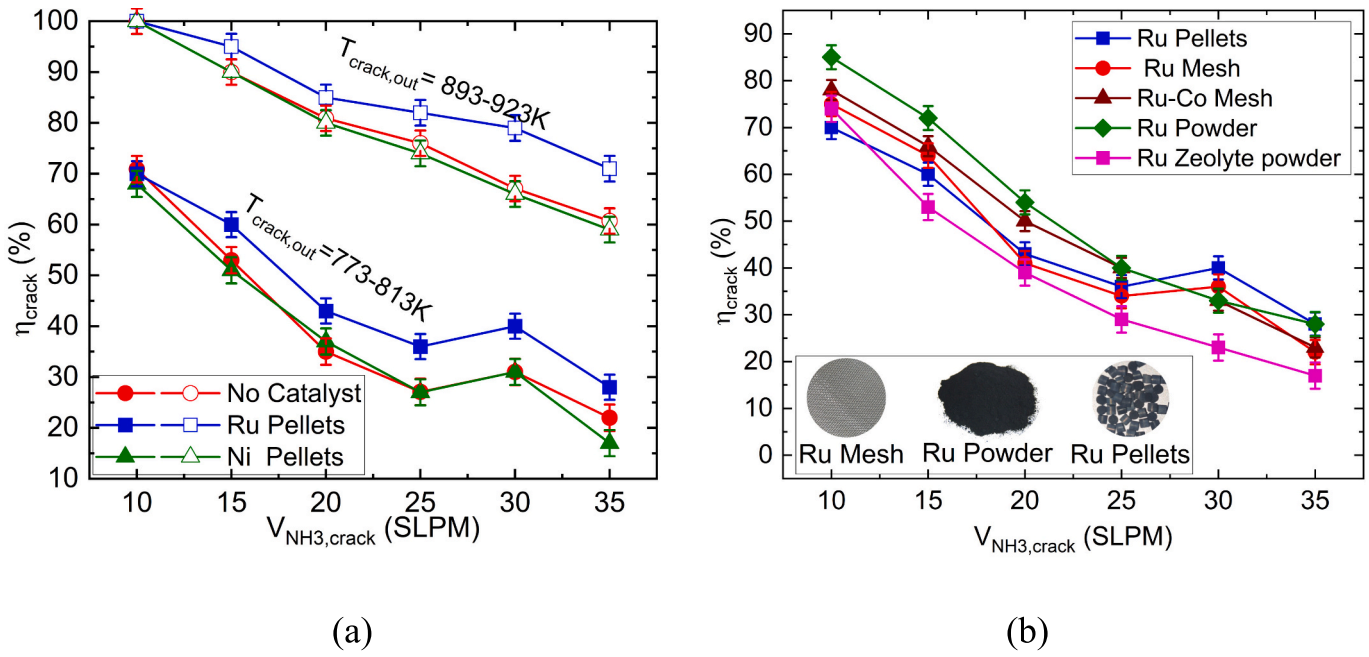

Fig. 5. Variation of cracking efficiency with NH_3 cracking flow rates for (a) different catalysts and (b) different configurations of Ru catalyst.

(Fig. 4 (a) & (b)). This could be due to the zeolite crystals being too large to capture this in imaging. If within large crystals, the channels may be misaligned and difficult to capture in images and lack proper formation. EDX mapping, as well as atomic contrast in HAADF images, confirms Ru presence in the Ru-Z samples (Fig. 4 (c) & (d)). Ru was observed as nanoparticles/clusters of atoms, instead of single atoms, and more often zeolite appears as an amorphous support. The elemental analysis of the separated liquid showed approximately 1000 mg/L Na presence, which confirms that most of the Na ions from the zeolite were replaced by Ru by ion exchange and the rest of the Ru were adsorbed as clusters of nanoparticles. Fig. 4 (e & f). shows the Ru particles appear at the edge of the zeolite support in 1–2 nm sizes.

3.1.2. *Impact of catalyst on the cracking efficiency*

The cracking efficiency (η_{crack}) refers to the volumetric ratio of cracked NH_3 to initial NH_3 concentration [7]. The cracker system was tested at different NH_3 flow rates ($V_{NH3,crack}$) at 773–813 K, and 893–932 K. Fig. 5 (a) compares pellet-based Ni (10 % Ni/Al_2O_3, Heraeus) and Ru (10 % Ru/Al_2O_3, Heraeus) catalysts to thermal cracking at these temperatures. The $\eta_{cracker}$ decreases from 70 % to 17 % at 773–813 K and from 100 % to 60 % at 893–932 K as NH_3 flow rate increases. As flow rates increase, NH_3 residence time in the cracker and catalyst tube decreases. The Ni catalyst had similar η_{crack} to thermal cracking, while the Ru-based catalyst had a 20 % increase at 35 Standard Litres Per Minute (SLPM) of NH_3 at 893–923 K.

Fig. 5(b) shows Ru catalyst experiments at 773–813 K using electroplated mesh, pellets, powders. Electroplated Ru and Ru—Co stainless steel mesh configurations produced similar results as the commercial catalysts. Since it was coated in thin layers, the coated wire mesh (Ru-mesh) contains little Ru compared to that of commercial catalysts, as

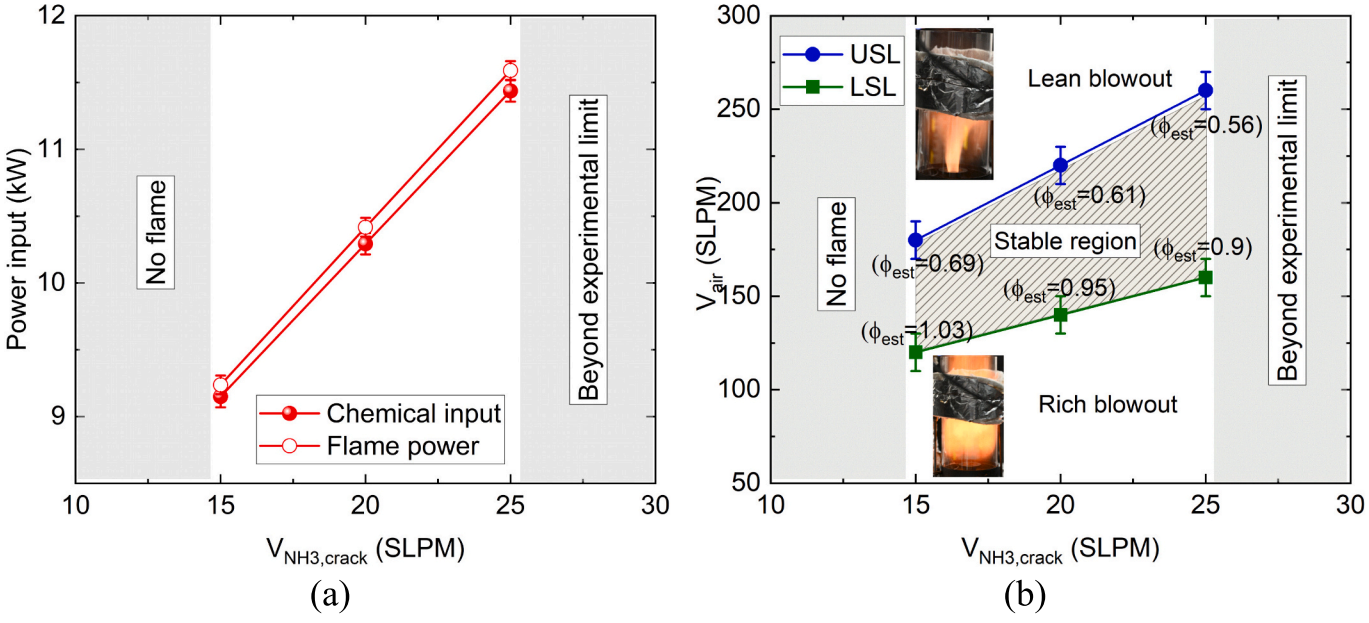

Fig. 6. Variation of (a) chemical input and (b) flame stability regime for different NH_3 cracking flow rates.

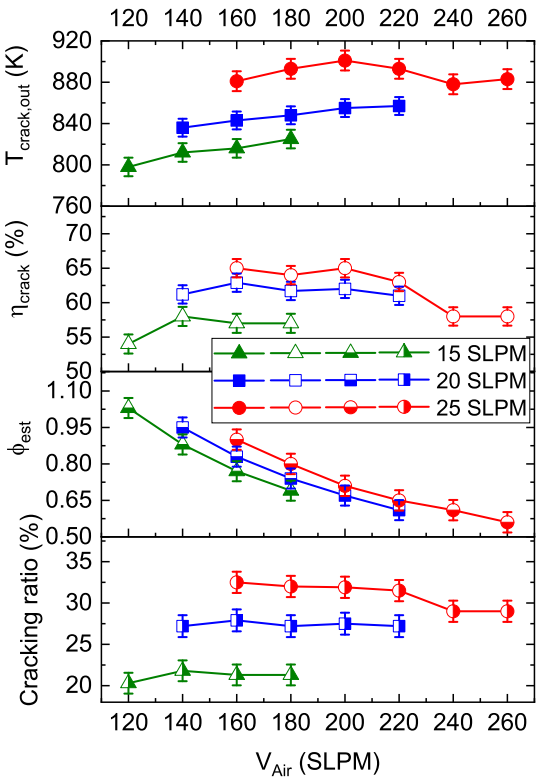

Fig. 7. Variation of cracking temperature, cracking efficiency of the cracker and estimated equivalence ratio and cracking ratio of the burner with air flow rates.

discussed in section 3.1. This indicates the need for more research to extend NH_3-Ru-coated wire-based catalyst interactions. It also highlights the implementation benefits to industry by achieving similar performance with a less expensive catalyst system, owing to the use of less mass of ruthenium which carries a high cost.

3.2. Combustion characteristics of in-situ cracked system

3.2.1. Static flame stability and cracking characteristics

The combustion performance of in-situ cracked flame was analysed for three $V_{NH3,crack}$ of 15 SLPM, 20 SLPM, and 25 SLPM, while maintaining the main NH_3 flow rate in the burner at 25 SLPM. These conditions correspond to NH_3 chemical inputs of 9.1 kW, 10.3 kW, and 11.4 kW, respectively. The chemical input was calculated as the product of the total NH_3 mass flow rate and its calorific value, whereas the flame power was determined as the sum of the product of NH_3 flow and its calorific value and the product of cracked H_2 flow and its calorific value. A lower chemical input results in insufficient cracking temperature, which is inadequate to sustain the flame due to poor η_{crack}, as indicated by the shaded region on the left side of Fig. 6(a) and (b). Conversely, achieving chemical input exceeding 11.4 kW is constrained by the NH_3 cylinder's inability to supply more than 50 SLPM throughout the experimental campaign. The results demonstrate that both chemical input and flame power increase linearly with an increase in $V_{NH3,crack}$. However, a slight increase of 1–1.4 % in flame power was observed due to the higher calorific value of H_2 in the resulted cracked mixture.

Fig. 6(b) illustrates the stability map of the burner for $V_{NH3,crack}$ of 15 SLPM, 20 SLPM, and 25 SLPM across a range of air flow rates (V_{air}). The stability map shifts towards higher V_{air} values owing to the linear increase in flame power. Notably, this shift corresponds to increases of 33 % and 44 % in the lower stability limit (LSL) and upper stability limit (USL), respectively, when the $V_{NH3,crack}$ = 25 SLPM as compared to the $V_{NH3,crack}$ = 15 SLPM. This shift can be attributed to the increase of cracking ratio in the combustor with the increase in $V_{NH3,crack}$ where the cracking ratio is defined as the percentage of H_2 present in the total reactant mixture within the burner.

The burner exhibits interesting instabilities onset of lean and rich blowout conditions. As V_{air} increases beyond the LSL, the flame becomes unstable, detaches from the burner rim, and transitions to wall-stabilized flames (as shown in the inset of Fig. 6(b)). Under these conditions, the cracking temperature decreases, leading to reduced production of H_2 and eventual flame blowout. On the lean side (beyond USL), the flame transitions into a jet-like structure (depicted in the inset of Fig. 6(b)), losing both inner and outer recirculation zones just before lean blowout occurs. A detailed analysis of flame morphology in cracked flame conditions is discussed in Section 3.2.2. However, a comprehensive dynamic stability analysis is necessary to gain deeper insights into these phenomena.

Furthermore, the cracking characteristic of the burner is studied in detail. The variation of temperature at the inlet of the catalytic tube (same as that of the outlet temperature of the cracker, $T_{crack,out}$), η_{crack}, the estimated equivalence ratio (ϕ_{est}) and the cracking ratio of the combustion with V_{air} are shown in Fig. 7. It is noteworthy that all these parameters are interdependent, such that even a slight change in one parameter can significantly influence the others. It is interesting to see that the $T_{crack,out}$ demonstrates approximately a constant trend of 810 ± 10, 850 ± 10 and 888 ± 10 K respectively, for 15 SLPM, 20 SLPM, and 25 SLPM, despite significant reductions in the ϕ_{est}.

The heat transfer to the cracker is strongly influenced by the

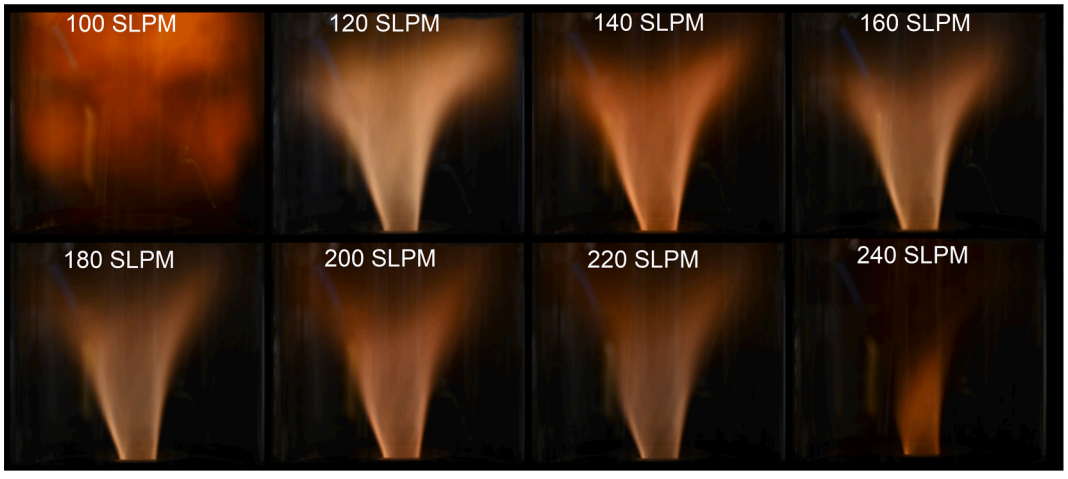

Fig. 8. Direct visualisation of cracked NH_3 flame for different air flow rates at NH_3 cracking flow rate of 20 SLPM.

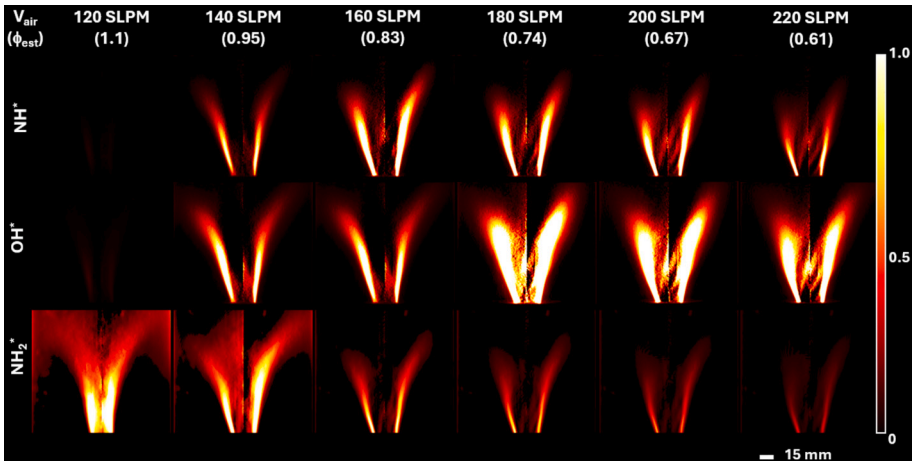

Fig. 9. Abel deconvoluted NH*, OH* and NH_2* chemiluminescence images of cracked NH_3 flame for different air flow rates at NH_3 cracking flow rate of 20 SLPM.

hydrodynamic characteristics of the flame. As the equivalence ratio decreases, the flame temperature drops; however, the convective heat transfer coefficient increases due to the rise in the Reynolds number [39]. This higher Reynolds number enhances turbulent mixing and improves heat exchange between the hot combustion gases and the NH_3 flowing through the heat exchanger. This interplay between flame temperature and bulk flow velocity explains the constant outlet temperature observed at the cracker outlet. However, a detailed numerical modelling of heat transfer analysis on the coupled cracker-burner system is needed to confirm these justifications. The η_{crack} decreased significantly from 65 % to 57 % when the V_{air} increased from 160 SLPM to 240 SLPM. This reduction can primarily be attributed to the lower flame temperature at $\phi_{est} = 0.6$ and the reduced residence time of NH_3 in the cracker at a higher NH_3 flow rate ($V_{NH3,crack} = 25$ SLPM).

Furthermore, $T_{crack,out}$, increases with an increase in $V_{NH3,crack}$, leading to a higher η_{crack}. For instance, when $T_{crack,out}$ rose from 816 K to 881 K, η_{crack} increased from 57 % to 65 % at an airflow rate of 160 SLPM. Although the V_{air} remained constant in both cases, the equivalence ratios were 0.77 and 0.9 for $V_{NH3,crack} = 15$ SLPM and 25 SLPM, respectively. This difference is primarily due to the increased cracking ratio of the burner inlet flow, which rose from 21.3 % to 32.5 %.

3.2.2. Flame morphology

The time-averaged broadband image of the cracked NH_3 flame for various air flow rates at $V_{NH3,crack} = 20$ SLPM is shown in Fig. 8. The flame structures observed at 15 SLPM and 25 SLPM closely resemble that at 20 SLPM and are therefore omitted for brevity. At 120 SLPM air, the flame exhibits a V-shaped structure initially, then eventually detaches and stabilises along the wall, similar to the flame shape shown for the 100 SLPM case in Fig. 8. This detachment ultimately leads to a rich blowout of the flame. The transition in flame structure is primarily attributed to the significant NH_3 slip, which lowers the cracking temperature and efficiency, thereby reducing the flame speed.

The flame remains well-anchored with a V-shaped profile for the range of V_{air} from 140 SLPM to 220 SLPM which is corresponding to $\phi_{est} = 0.95$ to 0.61. However, a progressive reduction in flame luminosity is observed, indicating a transition towards lean blowout conditions. At 240 SLPM, the vortex roll-up region largely disappears, leaving only a portion of the flame root visible. This results in a substantial increase in unburnt NH_3, leading to a reduction in the cracking temperature and, consequently, lean blowout. It should be noted that the colours in the captured images may not provide an accurate representation of flame properties, as radiative heat from the cracker positioned above the flame top can influence direct photographic observations.

The flame chemiluminescence images of NH*,OH* and NH_2* for different air flow rates are shown in Fig. 9. As the V_{air} increased, the ϕ_{est} decreased from 1.1 to 0.61. The intensity of NH_2* increases as the flame moves towards the rich side. Notably, the maximum intensity of NH_2* is observed at an ϕ_{est} of 0.95, which is 1.4 times higher than at 0.61. The increased intensity of NH_2* suggests a higher NH_3 content in the flame. Furthermore, the NH_2* emission broadens near the flame root, eventually leading to flame blowout due to the absence of OH, H, or O radicals necessary for further oxidation of NH_3 on the rich side.

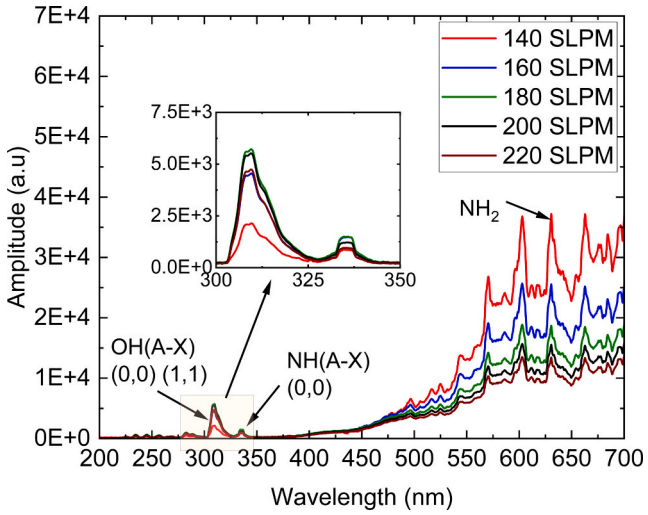

Fig. 10. Spectroscopic values of cracked NH_3 flame for different air flow rates at NH_3 cracking flow rate of 20 SLPM.

In contrast, OH* and NH* exhibit similar trends, with their maximum intensities occurring at equivalence ratios of 0.74 and 0.83, respectively, and decreasing on either side of the equivalence ratio. The peak intensity of OH* also indicates the presence of high-temperature regions, while the abundance of OH* facilitates the oxidation of NH_2 to NH, with the NH peak occurring at an equivalence ratio of 0.74. This shift is primarily due to the interplay between NH_2 and OH formation reactions.

This trend is further confirmed by the chemiluminescence spectrum in the wavelength range of 200 to 700 nm, as shown in Fig. 10. Measured intensities of OH* and NH* were found to be significantly lower than NH_2* across all conditions studied. A similar trend has been observed by previous researchers [11,38,40].

3.3. Global emission characteristics

The sampled volume fractions of NO, NO_2, N_2O, and NH_3 in the

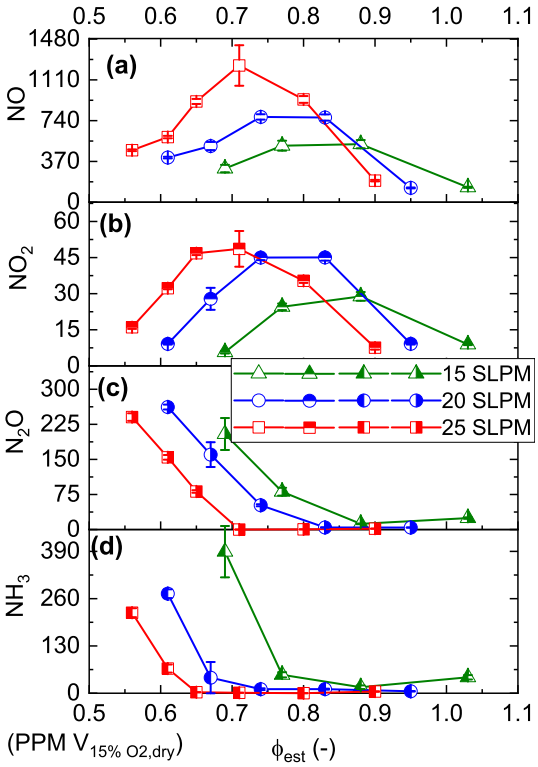

Fig. 11. Variation of (a) NO, (b) NO_2, (c) N_2O and (d) NH_3 with estimated equivalence ratio at NH_3 cracking flow rates of 15 SLPM, 20 SLPM and 25 SLPM.

combustion exhaust gas were analysed for different NH_3 cracker flow rates ($V_{NH3,crack}$ = 15 SLPM, 20 SLPM, and 25 SLPM). Although the experiment does not precisely control the equivalence ratio due to the combined effects of burner performance and the cracker system, the overall trend in the emission profiles can be approximated from Fig. 11. It is evident that the exhaust gas species follow a similar trend regardless of $V_{NH3,crack}$, with a slight shift towards leaner conditions as $V_{NH3,crack}$ increases. This shift is primarily attributed to the synergistic effects of heat loss, the burner's cracking ratio, and thermal power.

The NO is expected to peak at a ϕ_{est} of 0.77–0.83, 0.74–0.83, and 0.71–0.8 for the 15 SLPM, 20 SLPM, and 25 SLPM cases, respectively. Additionally, NO production is 47 % and 77 % higher for the 20 SLPM and 25 SLPM flow rates compared to the 15 SLPM case. This increase is attributed to the increase the production of radicals such as H, OH, NH, and O, which significantly enhance NO formation through interactions in the HNO pathway as the $V_{NH3,crack}$ increases.

It can be inferred that lower combustion efficiency contributes to lower NO emissions under fuel-lean conditions, as NO production is directly linked to NH_3 consumption. The combustion efficiency is defined as the ratio of the chemical energy released by the combustion of NH_3 and H_2 to the total chemical energy available in the fuel mixture [41]. Additionally, there may be lower NO production via HNO routes (e.g. OH + NH → HNO + H) due to lower flame temperatures at lean conditions. Following on from the reduced NH_2* intensity at lean conditions shown in Fig. 9, consumption of NO by NH_2 via the reaction NH_2 + NO → N_2 + H_2O may have been lower at ϕ_{est} = 0.74–0.83. These two factors could also explain the increase in NO emission with higher cracker flowrates – higher flame temperatures from the extra dissociated H_2 would increase NO production and reduced NH_2 and NH concentrations would consume less NO. The wall heat loss may also limit the formation of O/H radicals near the wall due to the temperature-sensitive nature of the major chain-branching reaction, H + O_2 → OH + O. The trend of NO_2 emissions mirrors that of NO, with enhanced NO oxidation under lean conditions.

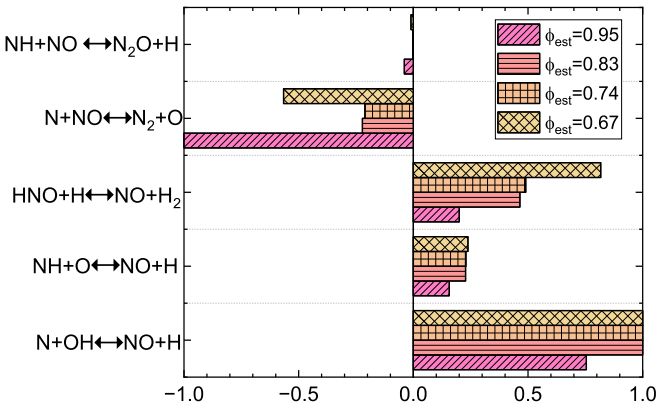

Fig. 12. Variation of absolute ROP of NO at the flame zone with different estimated equivalence ratios at NH_3 cracking flow rates of 20 SLPM.

A sharp increase in N_2O is observed at ϕ_{est} values of 0.88, 0.83, and 0.71 for 15 SLPM, 20 SLPM, and 25 SLPM, respectively. This is attributed to the enhanced NH concentration, which accelerates N_2O production by consuming NO [42]. Additionally, at 15 SLPM, more heat is lost to the cracker, resulting in a relatively cooler combustion environment that slows down the N_2O consumption reactions, which are temperature dependent. The unburned NH_3 follows a similar trend to that of N_2O.

Furthermore, a chemical reaction network (CRN) developed in the author's previous studies [11,35,36,42] has been employed to analyse the flame chemistry driving NO formation under various operating conditions utilizing the reaction mechanism proposed by Stagni et al. [43] for NH_3–H_2-air mixtures, which incorporates 31 chemical species and 203 reactions. The rate of production (ROP) of NO within the flame zone was analysed for different global equivalence ratios at a cracking flow rate of 20 SLPM, as illustrated in Fig. 12. To facilitate meaningful comparisons, the ROP values were normalised to their respective maximum values for each operating condition.

The two most significant reactions contributing to NO formation were identified as N + OH → NO + H and HNO + H → NO + H_2 for ϕ_{est} of 0.83, 0.74, and 0.67. These reactions are particularly prominent due to the high concentrations of OH* and NH*, which play a crucial role in promoting NO production. The presence of OH* facilitates the N + OH reaction pathway, while NH* enhances the formation of HNO, leading to the subsequent reaction with H. In contrast, for higher equivalence ratios, such as ϕ_{est} = 0.95, the dominant pathways of NO consumption reactions are N + NO → N_2 + O and NH + NO → N_2O + H, which become significant due to the increased availability of NH_2*. The presence of NH_2 promotes the NH + NO reaction, leading to the formation of N_2O, thereby reducing the overall NO concentration. This is particularly effective for ϕ_{est} = 0.95 as the higher flame temperatures at near-stoichiometric conditions facilitate the decomposition of this N_2O into molecular nitrogen via the reaction N_2O + H → N_2 + OH.

Furthermore, the reaction pathway of NH_3 combustion, as illustrated in Fig. 13, begins with NH_3 and terminates with NO. In this analysis, the maximum number of species displayed is limited to 10, with a minimum relative cutoff fraction of 5 %. A comparative study was conducted at ϕ_{est} = 0.95 and 0.74 to investigate differences in reaction behaviour. Overall, the global reaction pathway remains largely unchanged between the two conditions. The NH_3undergoes stepwise oxidation by OH radicals, forming key intermediate species such as NH_2, NH, HNO, and NO. The primary formation route of NO involves the reactions HNO → H + NO and HNO + H → NO + H_2, which together contribute approximately 40 % to the total NO production. At ϕ_{est} = 0.95, the reaction NH + NH_2 → N_2H_2+ H accounts for about 16 % of NH consumption. This is closely related to the higher NH_3 concentration under this condition compared to that at an equivalence ratio of 0.74. Meanwhile, increased

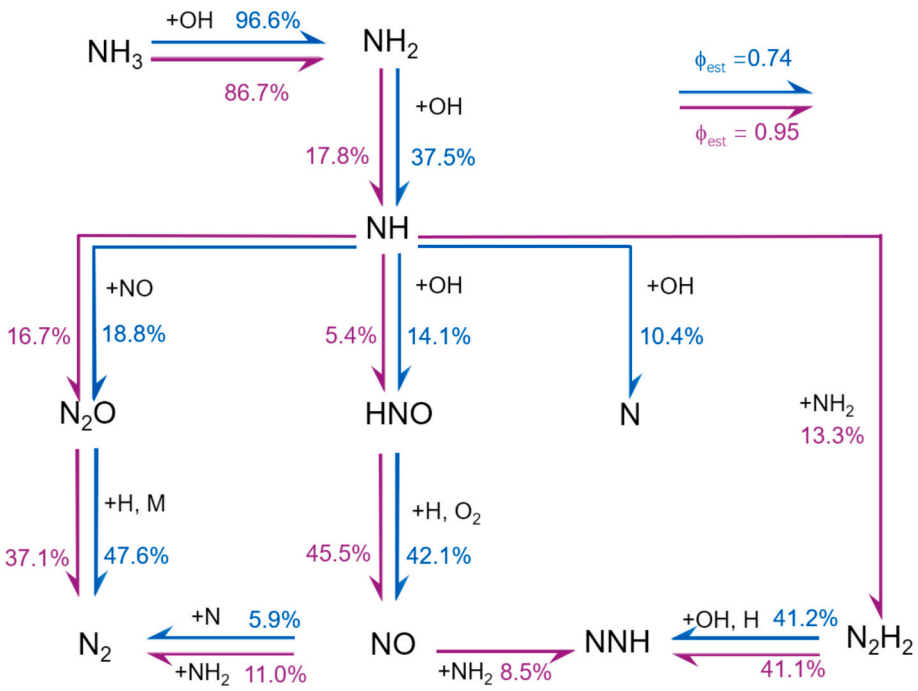

Fig. 13. The main reaction scheme in flame zones at ϕ_{est} = 0.95 and 0.74 with NH_3 cracking flow rates of 20 SLPM.

concentrations of NH_2 and NH radicals enhance the consumption of NO through reactions leading to the formation of NNH, N_2, and N_2O.

4. Conclusion

This study has successfully demonstrated the feasibility of in-situ thermo-catalytic cracking of NH_3 using a novel multi-pass heat exchanger cracker system. The key conclusions are summarized as follows:

(1) The Ru-based catalysts, particularly those electroplated on stainless steel wire mesh, exhibited superior performance in terms of cracking efficiency compared to thermal cracking alone. The Ru and Ru—Co electroplated stainless steel mesh configuration showed similar performance to commercially available catalysts, highlighting the potential for a cost-effective catalyst system with reduced ruthenium usage in the Ru-mesh.
(2) The cracked flame demonstrated a wide range of flame stability across three NH_3 flow rates ($V_{NH3,crack}$ = 15 SLPM, 20 SLPM, and 25 SLPM). Distinct flame instabilities and morphologies were observed at the onset of lean and rich flame blowouts.
(3) The combustion characteristics of the cracked flame revealed interdependencies among the inlet temperature of the catalytic tube ($T_{crack,out}$), cracking efficiency (η_{crack}), estimated equivalence ratio (ϕ_{est}), and the cracking ratio of the combustion process. Even minor changes in one parameter significantly influenced the other.
(4) The emission showed a similar trend across different $V_{NH3,crack}$, with a slight shift towards leaner conditions as $V_{NH3,crack}$ increased. This shift was driven by synergistic effects of heat loss, the burner's cracking ratio, and thermal power. Optimizing catalyst contact time and enhancing flame stability are critical for improving performance and reducing emissions.
(5) The NO emissions peaked at ϕ_{est} ranges of 0.77–0.83, 0.74–0.83, and 0.71–0.80 for the 15 SLPM, 20 SLPM, and 25 SLPM cases, respectively. NO production was 47 % and 77 % higher for the 20 SLPM and 25 SLPM cases compared to 15 SLPM, primarily due to increased radical production (H, OH, NH, and O), which enhanced NO formation via the HNO pathway. These findings were further validated through detailed CRN analysis.

The narrow stability limits, low cracking efficiency at higher NH_3 flow rates and poor experimental flexibility in controlling the various parameters of the present in-situ cracked flame open the scope for future study. A comprehensive investigation into the development of low-cost, high-performance catalysts and improved cracker designs is essential for further advancement of this system. Furthermore, the promising results obtained with the Ru-based catalysts suggest that further optimisation and scaling up of this technology could contribute significantly to advancing sustainable combustion technologies and reducing reliance on fossil fuels.

CRediT authorship contribution statement

B. Aravind: Writing – original draft, Methodology, Investigation, Formal analysis, Data curation, Conceptualization. **Sivachidambaram Sadasivam:** Writing – review & editing, Methodology, Investigation, Data curation. **Jordan Davies:** Writing – review & editing. **Syed Mashruk:** Writing – review & editing, Supervision, Funding acquisition, Conceptualization. **Agustin Valera-Medina:** Writing – review & editing, Supervision, Resources, Conceptualization.

Declaration of competing interest

The authors declare that they have no known competing financial interests or personal relationships that could have appeared to influence the work reported in this paper.

Acknowledgement

This work was supported by the AMBURN project with funding from the Department for Energy Security and Net Zero (DESNZ) (Grant Number: IFS2–06-FLO). The research was undertaken at Cardiff University's Thermofluids Lab (W/0.17) with invaluable technical support from Mr. Jonathan Martin. The authors would like to thank Heraeus Precious Metals for providing catalysts used in the cracking

experiments. The authors are grateful to Ella Kitching and Dr. Nicola Emmerson for their help with TEM and FTIR measurements. Information on the data underpinning this publication, including access details, can be found in the Cardiff University Research Data Repository at https://doi.org/10.17035/cardiff.30126730.

Data availability

Data will be made available on request.

References

[1] Valera-Medina A, Xiao H, Owen-Jones M, David WI, Bowen P. Ammonia for power. Prog Energy Combust Sci 2018;69:63–102.
[2] Elbaz AM, Wang S, Guiberti TF, Roberts WL. Review on the recent advances on ammonia combustion from the fundamentals to the applications. Fuel Commun 2022;10:100053.
[3] Kobayashi H, Hayakawa A, Somarathne KKA, Okafor EC. Science and technology of ammonia combustion. Proc Combust Inst 2019;37:109–33.
[4] Verkamp F, Hardin M, Williams J. Ammonia combustion properties and performance in gas-turbine burners. Symposium (International) on combust. Elsevier; 1967. p. 985–92.
[5] Morlanés N, Katikaneni SP, Paglieri SN, Harale A, Solami B, Sarathy SM, et al. A technological roadmap to the ammonia energy economy: Current state and missing technologies. Chem Eng J 2021;408:127310.
[6] Ti S, Chen Z, Li Z, Kuang M, Xu G, Lai J, et al. Influence of primary air cone length on combustion characteristics and NOx emissions of a swirl burner from a 0.5 MW pulverized coal-fired furnace with air staging. Appl Energy 2018;211:1179–89.
[7] Devkota S, Cha J-Y, Shin B-J, Mun J-H, Yoon HC, Mazari SA, et al. Techno-economic and environmental assessment of hydrogen production through ammonia decomposition. Appl Energy 2024;358:122605.
[8] Jano-Ito M, Valera-Medina A. Techno-economics of ammonia as an energy carrier. Exporting wind from the North Atlantic Ocean/North Sea to Wales. J Ammonia Energy 2024:2.
[9] Alnajideen M, Shi H, Northrop W, Emberson D, Kane S, Czyzewski P, et al. Ammonia combustion and emissions in practical applications: a review. Carbon Neutrality 2024;3:1–45.
[10] Mashruk S, Shi H, Mazzotta L, Ustun CE, Aravind B, Meloni R, et al. Perspectives on NO X Emissions and Impacts from Ammonia Combustion Processes. Energy Fuel 2024;38:19253–92.
[11] Mashruk S, Kovaleva M, Alnasif A, Chong CT, Hayakawa A, Okafor EC, et al. Nitrogen oxide emissions analyses in ammonia/hydrogen/air premixed swirling flames. Energy 2022;260:125183.
[12] Wang S, Chong CT, Xie T, Józsa V, Ng J-H. Ammonia/methane dual-fuel injection and Co-firing strategy in a swirl flame combustor for pollutant emissions control. Energy 2023;281:128221.
[13] Kikuchi K, Murai R, Hori T, Akamatsu F. Fundamental study on ammonia low-NOx combustion using two-stage combustion by parallel air jets. Processes 2021;10:23.
[14] Li Z, Li S. Effects of inter-stage mixing on the NOx emission of staged ammonia combustion. Int J Hydrog Energy 2022;47:9791–9.
[15] Han X, Wang Z, He Y, Liu Y, Zhu Y, Konnov AA. The temperature dependence of the laminar burning velocity and superadiabatic flame temperature phenomenon for NH3/air flames. Combustion Flame 2020;217:314–20.
[16] Liang W, Law CK. Enhancing ammonia combustion using reactivity stratification with hydrogen addition. Proc Combust Inst 2023;39:4419–26.
[17] Aravind B, Yu L, Lacoste D. Enhancement of lean blowout limits of swirl stabilized NH3-CH4-Air flames using nanosecond repetitively pulsed discharges at elevated pressures. Appl Energy Combustion Sci 2023;16:100225.
[18] Valera-Medina A, Marsh R, Runyon J, Pugh D, Beasley P, Hughes T, et al. Ammonia–methane combustion in tangential swirl burners for gas turbine power generation. Appl Energy 2017;185:1362–71.
[19] Tu Y, Zhang H, Guiberti TF, Jimenez CDA, Liu H, Roberts WL. Experimental and numerical study of combustion and emission characteristics of NH3/CH4/air premixed swirling flames with air-staging in a model combustor. Appl Energy 2024;367:123370.
[20] Chai WS, Bao Y, Jin P, Tang G, Zhou L. A review on ammonia, ammonia-hydrogen and ammonia-methane fuels. Renew Sust Energ Rev 2021;147:111254.
[21] Asif M, Bibi SS, Ahmed S, Irshad M, Hussain MS, Zeb H, et al. Recent advances in green hydrogen production, storage and commercial-scale use via catalytic ammonia cracking. Chem Eng J 2023;473:145381.
[22] Realpe N, Lezcano G, Kulkarni SR, Sayas S, Morlanes N, Rakib M, et al. The technological prospects of repurposing methane steam reformers into ammonia crackers for decarbonized H2 production. Appl Energy 2024;376:124244.
[23] Yang G, Guo H, Kang Z, Zhao L, Feng S, Jiao F, et al. Green Hydrogen Separation from Nitrogen by Mixed-Matrix Membranes Consisting of Nanosized Sodalite Crystals. ChemSusChem 2019;12:4529–37.
[24] Davies J, Mashruk S, Sato D, Mazzotta L, Pugh D, Valera-Medina A. Emissions analyses of humidified cracked ammonia swirling flames. Combustion Flame 2025;274:113984.
[25] Meng X, Liu L, Qin M, Miao M, Zhao H, Long W, et al. Study on ammonia/methanol blends with ammonia cracking for low-carbon combustion and NO reduction. J Clean Prod 2024;450:141959.
[26] An Z, Zhang W, Zhang M, Xing J, Kai R, Lin W, et al. Experimental and Numerical Investigation on Combustion Characteristics of Cracked Ammonia Flames. Energ Fuels 2024;38:7412–30.
[27] Asif M, Bibi SS, Ahmed S, Irshad M, Hussain MS, Zeb H, et al. Recent advances in green hydrogen production, storage and commercial-scale use via catalytic ammonia cracking. Chem Eng J 2023;145381.
[28] Wu Z-W, Li X, Qin Y-H, Deng L, Wang C-W, Jiang X. Ammonia decomposition over SiO2-supported Ni–Co bimetallic catalyst for COx-free hydrogen generation. Int J Hydrog Energy 2020;45:15263–9.
[29] Li L, Chen F, Dai Y, Wu J, Shao JL, Li HY. Fe-assisted Ru clusters supported on porous and graphitic carbon for ammonia decomposition to COx free hydrogen. RSC Adv 2016;6:102336–42.
[30] Su Z, Guan J, Liu Y, Shi D, Wu Q, Chen K, et al. Research progress of ruthenium-based catalysts for hydrogen production from ammonia decomposition. Int J Hydrog Energy 2024;51:1019–43.
[31] Edison TNJI, Atchudan R, Karthik N, Chandrasekaran S, Perumal S, Raja PB, et al. Deep eutectic solvent assisted electrosynthesis of ruthenium nanoparticles on stainless steel mesh for electrocatalytic hydrogen evolution reaction. Fuel 2021;297:120786.
[32] Ma X, Ma Y, Li H, Tian Y. Deposition of Selective Catalytic Reduction Coating on Wire-Mesh Structure by Atmospheric Plasma Spraying. Materials 2019;12:3046.
[33] Leung KC, Hong S, Li G, Xing Y, Ng BKY, Ho P-L, et al. Confined Ru Sites in a 13X Zeolite for Ultrahigh H2 Production from NH3 Decomposition. J Am Chem Soc 2023;145:14548–61.
[34] Aceto D, Bacariza MC, Travert A, Henriques C, Azzolina-Jury F. Thermal and Plasma-Assisted CO2 Methanation over Ru/Zeolite: A Mechanistic Study Using In-Situ Operando FTIR. Catalysts 2023;13:481.
[35] Sato D, Davies J, Mazzotta L, Mashruk S, Valera-Medina A, Kurose R. Effects of Reynolds number and ammonia fraction on combustion characteristics of premixed ammonia-hydrogen-air swirling flames. Proc Combust Inst 2024;40:105283.
[36] Mashruk S, Alnasif A, Yu C, Thatcher J, Rudman J, Peronski L, et al. Combustion Characteristics of a Novel Ammonia Combustor equipped with Stratified Injection for Low Emissions. J Ammonia Energy 2023;1:21–32.
[37] Gaydon A. The spectroscopy of flames: springer science & business media. 2012.
[38] Dasch CJ. One-dimensional tomography: a comparison of Abel, onion-peeling, and filtered backprojection methods. Appl Opt 1992;31:1146–52.
[39] Aravind B, Hiranandani K, Kumar S. Development of an ultra-high capacity hydrocarbon fuel based micro thermoelectric power generator. Energy 2020;206:118099.
[40] Wei Y, Zhu X, Tian B, Zhou H, Issayev G, Cheng Y-B, et al. Excited Species as Heat Release Rate Markers in Laminar Premixed Ammonia–Hydrogen–Air Flames. Energy Fuel 2024;38:11311–20.
[41] Kim JH, Song JH, Ku JW, Kim YH, Kwon OC. Combustion characteristics of premixed ammonia-hydrogen/air flames in a swirl model combustor. Int J Hydrog Energy 2024;49:1075–86.
[42] Mashruk S, Okafor E, Kovaleva M, Alnasif A, Pugh D, Hayakawa A, et al. Evolution of N2O production at lean combustion condition in NH3/H2/air premixed swirling flames. Combustion Flame 2022;244:112299.
[43] Stagni A, Cavallotti C, Arunthanayothin S, Song Y, Herbinet O, Battin-Leclerc F, et al. An experimental, theoretical and kinetic-modeling study of the gas-phase oxidation of ammonia. Reaction Chem Eng 2020;5:696–711.